



Radio Science



RESEARCH ARTICLE

10.1029/2020RS007169

Key Points:

- Radio emissions from the electrical grid act as a widespread illumination source for imaging sporadic E
- The technique described in this paper enables tracking and mapping of sporadic E structures
- Since the source of RF is broadband, this method may also enable tracking of sporadic E electron density

Supporting Information:

- · Supporting Information S1
- · Movie S1

Correspondence to:

K. S. Obenberger, obenken@icloud.com

Citation:

Obenberger, K. S., Dowell, J., Fallen, C. T., Holmes, J. M., Taylor, G. B., & Varghese, S. S. (2021). Using broadband radio noise from power-lines to map and track dense *E_s* structures. *Radio Science*, *56*, e2020RS007169. https://doi.org/10.1029/2020RS007169

Received 21 JUL 2020 Accepted 20 DEC 2020

© 2020. The Authors. This is an open access article under the terms of the Creative Commons Attribution License, which permits use, distribution and reproduction in any medium, provided the original work is properly cited.

Using Broadband Radio Noise From Power-Lines to Map and Track Dense E_s Structures

K. S. Obenberger¹, J. Dowell², C. T. Fallen¹, J. M. Holmes¹, G. B. Taylor², and S. S. Varghese²

¹Space Vehicles Directorate, Air Force Research Laboratory, Kirtland AFB, NM, USA, ²University of New Mexico, Albuquerque, NM, USA

Abstract We present passive observations of midlatitude sporadic E (E_s) structures in the 30–50 MHz range using the long wavelength array telescopes in New Mexico. Spectral and temporal analysis of the structures reveals that some of the emissions can be characterized by broadband, spark-like radiation occurring at a repetition frequency of 60 Hz. The azimuthal distribution indicates that the brightest emissions come from the directions of several large metropolitan centers with distances ranging from 700 to 1,250 km from the telescopes. This implies that the source is unintended human-made noise, originating from devices connected to 60 Hz alternating current power. The geometry of our observations rule out coherent scatter from field-aligned irregularities, and indicate that the unintended noise must undergo a specular reflection off of over-dense plasma distributed approximately parallel to Earth's surface. On certain occasions the reflections are seen at such high frequencies and high elevation angles that the local plasma frequency must be above 30 MHz. During both day and night E_s conditions, the dense structures are observed to be arranged in propagating fronts, and travel at speeds of 70–100 m/s. We also present observations that reveal quasi-periodic amplitude oscillations with frequencies consistent with atmospheric gravity waves and acoustic waves.

Plain Language Summary Dense, patchy layers of plasma that form in the E layer of the ionosphere (sporadic E) often reflect high frequency radio waves from distant, over-the-horizon sources. While detectable with current radar techniques, sporadic E is difficult to image over large regions due to the limited field of view of a typical radar. We show that unintentional, human-made radio emissions, originating from the electrical grid, act as a widespread set of radio sources, with hotspots centered on large metropolitan areas. The radio emissions reflect off of sporadic E plasma and are readily detectable and imaged by radio telescopes such as the Long Wavelength Array (LWA) in New Mexico. We present LWA observations that prove this capability, which enables the tracking and mapping of sporadic E over large regions.

1. Introduction

The general consensus on the formation of midlatitude Sporadic E (E_s) is that when a shear exists in the neutral wind, drifting ions can pull electrons into a thin layer for two geometries. In the meridional case, a northern or southern wind can create vertical drift along the magnetic field lines, such that at a shear, ions from above drift down and electrons from below drift up, forming a thin, dense layer of plasma. In the zonal case, a western or eastern wind can create a $\vec{V} \times \vec{B}$ drift moving ions up or down, such that at a shear, ions may collect in a thin layer, where \vec{V} is the neutral wind vector and \vec{B} is the geomagnetic field vector. The plasma frequency of these layers can oftentimes be many times greater than foF2 (the peak frequency of the F layer) (Haldoupis, 2012; Mathews, 1998; Whitehead, 1960, 1970, 1989). E_s has long been known to enable long distance very high frequency (VHF; 30–300 MHz) communication, where extremely dense regions of E_s plasma reflect radio signals that would otherwise pass through the ionosphere.

Plasma instability simulations indicate that E_s forms in frontal structures that prefer a NW-SE orientation and typically travel to the South (Cosgrove & Tsunoda, 2002, 2004; Yokoyama & Stolle, 2016; Yokoyama et al., 2009). These models explain coherent scatter radar observations of nighttime field aligned irregularities (FAIs), which revealed frontal structures aligned NW-SE that are associated with E_s (Chu & Wang, 1997; D. L. Hysell & Burcham, 2000; D. L. Hysell et al., 2010; D. L. Hysell et al., 2004; Saito et al., 2006; M. Yamamoto

OBENBERGER ET AL. 1 of 17



et al., 1994). Global positioning system (GPS) observations of total electron content by Maeda and Heki (2013, 2015) confirmed the conclusions drawn from earlier radar studies, showing detailed maps of both day and nighttime E_s structures forming and propagating in long frontal structures.

While extremely useful for studying the orientation of E_s fronts, neither GPS-TEC nor coherent scatter radar can provide the density of the E_s plasma. Typically, this information is derived from high frequency (3–30 MHz; HF) radar. HF radars, such as Ionosondes, step through the HF band and measure the returns as a function of frequency. The peak frequency of a E_s layer (fo E_s) can be determined by the maximum reflected frequency. Ionosondes, however, typically do not have the imaging capabilities necessary to capture the morphology of E_s , rather they observe the select portions of the sky where the geometry is right for reflection, and for most cases, this is vertical sounding only.

Geospatial measurements of fo E_s , where the density is measured across frontal structures could provide key information for verifying E_s formation models. For instance in addition to the plasma instability mechanism mentioned above, Larsen (2000) and Bernhardt (2002) show the Kelvin-Helmholtz turbulence can produce intense modulations of E_s on size scales of a few km. Moreover, atmospheric gravity waves have been shown to play a key role in E_s formation and modulation (Didebulidze & Lomidze, 2010; Liu et al., 2014; Woodman et al., 1991). Instruments that are able to map the electron density would be highly valuable for determining the importance of each mechanism.

The two long wavelength array (LWA) radio telescopes in New Mexico, each with 256 dual-polarization dipole antennas, are capable of high resolution imaging in the HF and VHF bands. These capabilities have enabled previous studies of high resolution ionospheric radar imaging (Helmboldt, 2016, Helmboldt et al., 2014, Helmboldt & Taylor, 2020; Malins et al., 2019; Obenberger et al., 2019). While these studies have focused on a single propagation channel or FAI imaging, an adequate number of distant radiators could enable mapping of ionospheric structure while enabling ionosonde-like determination of foE_s in many directions simultaneously.

In this paper, we present completely passive, all-sky imaging observations from the LWA in the VHF band. Our observations reveal dense plasma structures consistent with E_s in climatology and morphology and may provide the ability to map and track fo E_s over large regions. The paper is organized as follows: Section 2 introduces the instruments and describes the observations used in this study, Section 3 describes the analysis carried out, and Section 4 discusses our finding and presents our conclusions.

2. Instruments and Data

With a wide field of view and good spatio-temporal resolution, recently constructed radio telescopes such as the LWA provide a viable alternative to traditional transmit/receive ionospheric observatories. Currently, there are two LWA radio telescopes located in central New Mexico. The first station, LWA1, is co-located with the Very Large Array and has been operating since 2011 (Ellingson et al., 2013). The second station, LWA-SV, is located 75 km NE of LWA1 at Sevilleta National Wildlife refuge and has been operating since 2016 (Cranmer et al., 2017). Each station consists of 256 dual-polarization dipole antennas that have been pseudo randomly placed within a 100×110 meter ellipse, and both stations are capable of digital beamforming as well as synthetic aperture imaging, where all of the elements are used as an interferometer allowing for all-sky imaging. LWA1 operates between 10 and 88 MHz, whereas LWA-SV, having slightly different analog receiver boards, can operate as low as 3 MHz. For this experiment, we make use of the all-sky imaging capabilities of both stations in the 30–50 MHz range.

Both LWA1 and LWA-SV are equipped with a LWA All-Sky Imager (LASI) backend, which correlates and images a narrowband (100 kHz) stream of voltages from each antenna (Obenberger et al., 2015). LASI is capable of correlating and imaging these data in real time, reducing a data rate of 357 GB/hr to 180 MB/hour. At each station, LASI is typically tuned to 38 MHz and creates 5 s all-sky images in near real time. Both stations have been uploading these images to a permanent archive, which can be found at http://lda10g.alliance.unm.edu. In addition to LASI, LWA-SV is equipped with a graphics processing unit correlator, which is capable of correlating and imaging a live stream of 20 MHz bandwidth from each antenna, producing images with 198 frequency bins. Continuous operation of this mode only began in late 2019. Due to the large size of the

OBENBERGER ET AL. 2 of 17

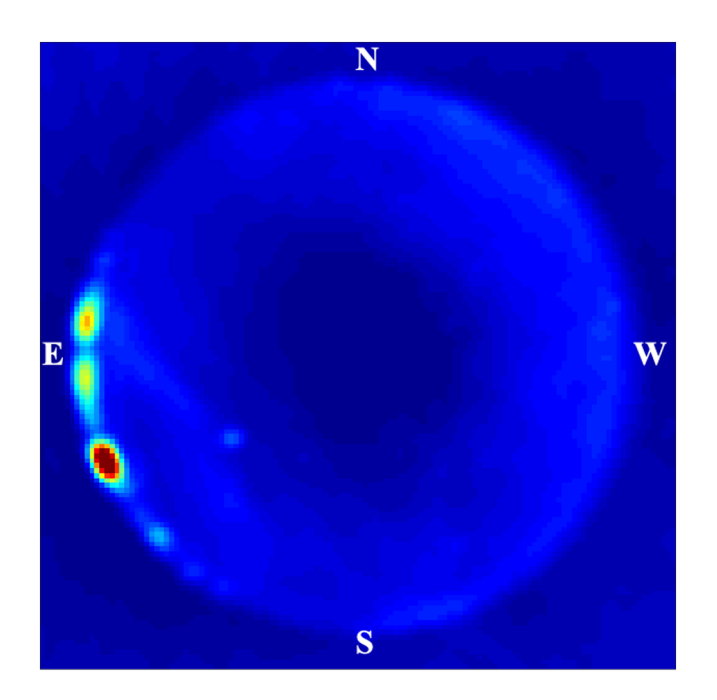


Figure 1. (Left) An example all-sky image from LWA-SV showing structures observed to the east and southeast on April 16, 2020.

broadband images, the images are temporarily stored to a rolling buffer of about a month.

To date, LASI at LWA1 has archived over 35,000 h of all-sky images dating back to March of 2012, and LWA-SV has archived 18,000 h dating back to May 2016. The addition of the LWA-SV imager allows for stereoscopic views of the local ionosphere. For this paper, we use LASI data captured between March 1, 2018 and February 29, 2020 and broadband imager data collected in April of 2020.

In addition to LWA, we also downloaded data from two Digisondes (Reinisch et al., 2009) located in Austin, TX and Boulder, CO using the Lowell Digisonde International data archive (http://giro.uml.edu). Each Digisonde (digital ionosonde) is capable of producing electron density profiles of the bottomside ionosphere from ionograms and detecting E_s . For this paper, we use a set of ionograms captured every 5 min between March 1, 2018 and February 29, 2020.

3. Analysis

Dating back to the early days of LWA1 operation, users of the LASI image data noticed that on occasion, distinct "structures" of radiation appeared along the horizon of the all-sky images. The structures were characterized by bright drifting emission at low elevation angles with spectra typically broader than the 100 kHz LASI bandwidth and slowly varying brightness lasting up to a few hours. The structures would often times appear to be oriented along a line (or front). These structures have been observed at all of the historical LASI operating frequencies, which ranged from 25 to 74 MHz.

The hypothesis was that the structures were an ionospheric effect and likely related to E_s , due to the very high frequencies observed and the fact that the structures appeared to be more common in the days surrounding the summer solstice, a climatology known to E_s (Whitehead, 1989). Figure 1 shows an example all-sky image at 38 MHz, where structures can be seen in the east and southeast near the horizon.

3.1. Analysis: Connection to E_s

To test a connection between the structures and E_s , we conducted a comparative study using the observed occurrence of the phenomena as seen from a LWA station and the measurement of foE_s as measured by the Digisondes at Austin and Boulder. The foE_s values for each Digisonde is calculated using the automatic ionogram scaling system (ARTIST) software (Reinisch & Huang, 1983). While it often appears to underestimate the actual foE_s , it is fairly reliable as a binary (yes or no) indicator of E_s . For instance, Figure 2 shows an ionogram from Austin, TX, on June 20, 2019, during sporadic E conditions. O-mode returns can be seen clearly up to 14 MHz, however ARTIST finds foE_s to be 9.9 MHz, where there is a break in the spectrum due to a protected band for WWV at 10 MHz. Despite this underestimate, ARTIST has accurately identified the existence of E_s . We also note that the apparent peak at 14 MHz, may actually be due to the roll-off of antenna gain, and foE_s could indeed be higher but not detectable.

Figure 3 shows the fo E_s as measured from Austin and Boulder for 10 consecutive days in April 2018. For most of the time, the strongest feature is the expected diurnal variation of the E region, with peak frequency up to 4 MHz at midday. However, Figure 3 shows several large jumps well above the diurnal variations, and these jumps indicate E_s activity. We regard an ARTIST estimated fo E_s above 5 MHz to be a possible case of E_s .

Both Digisondes produce an ionogram (and an fo E_s estimate) once every 5 min. The percentage of a given day where E_s activity is observed can be estimated by summing the number of ionograms with fo $E_s > 5$ MHz

OBENBERGER ET AL. 3 of 17

10.1029/2020RS007169

ShowIonogram v 1.0

100

5.8

MUF

200

5.9

400

6.1

600

6.5

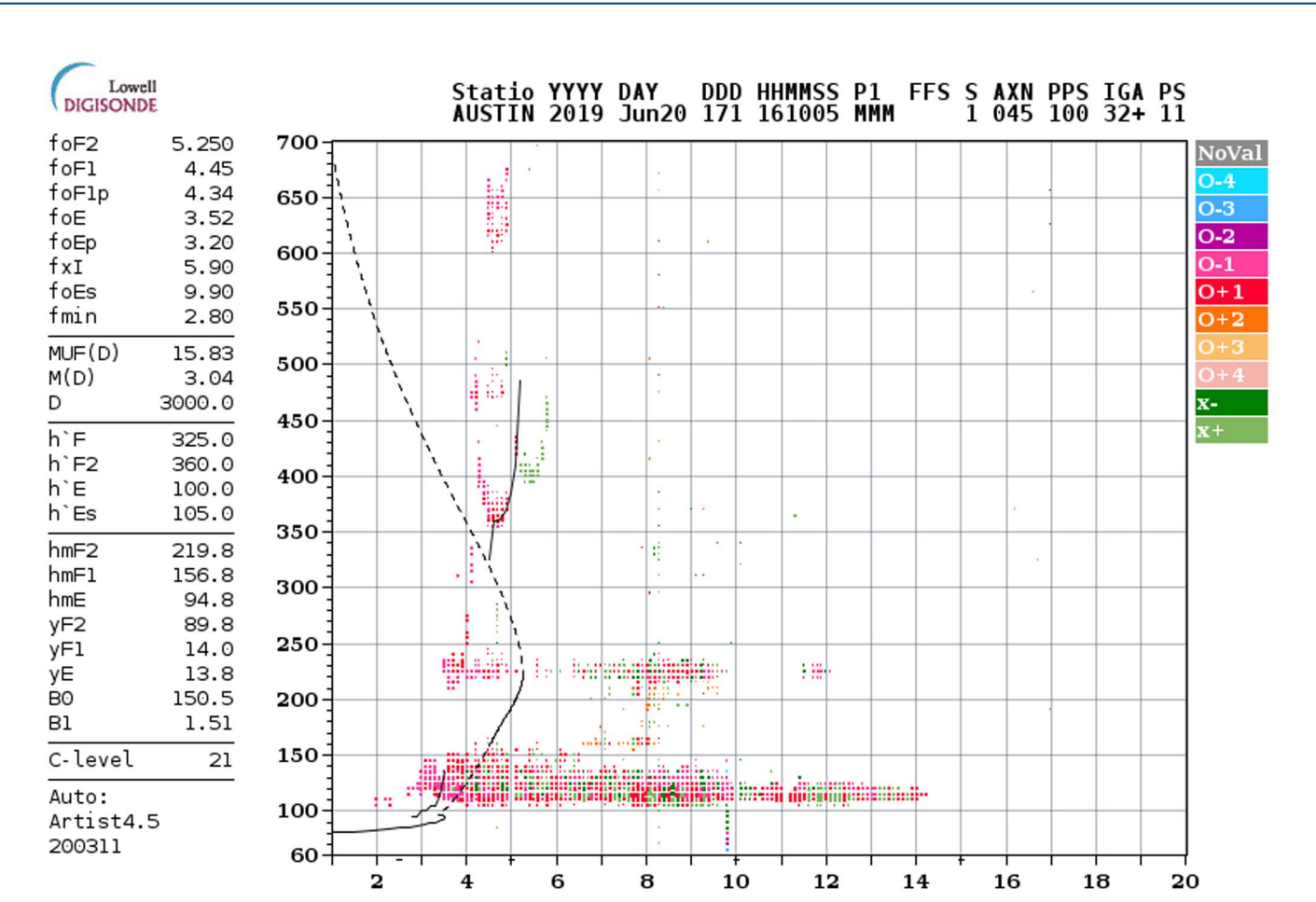


Figure 2. An ionogram recorded by the Digisonde in Austin, TX on June 20, 2019. Note that while O-mode returns exist up to 14 MHz, ARTIST finds fo E_s to be 9.9 MHz, where there is a break in the spectrum due to a protected band for WWV at 10 MHz.

800 1000 1500 3000 [km] 7.0 7.8 10.1 15.8 [MHz]

35276946.tmp / 190fx128h 100 kHz 5.0 km / DGS-256 AU930 130 / 30.4 N 262.3 E

and dividing by 288 (the number of 5 min intervals in 24 h). Analyzing these data over the course of a year or more for the Austin and Boulder digisondes provides a picture of the climatology of E_s in the southwestern region of the US, which can then be compared to the occurrence of the LWA observed phenomenon.

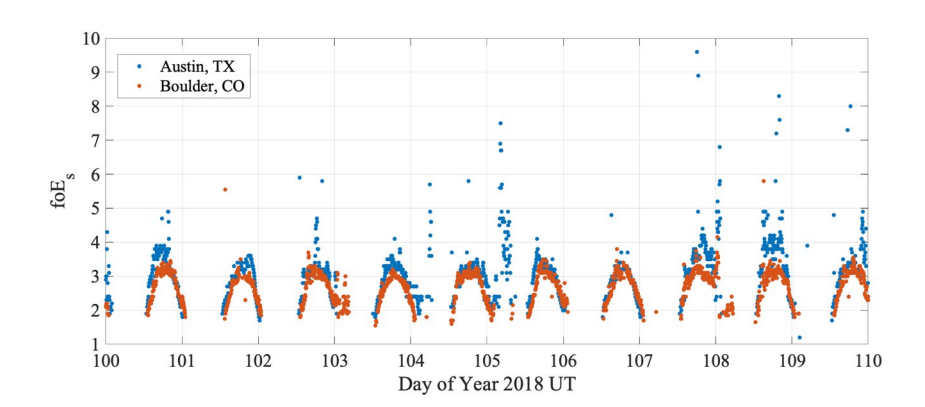


Figure 3. A plot showing either foE, or when observed foE_s. Observations are shown for the Digisondes in Austin (Blue) and Boulder (Red) in April 2018. Note the diurnal variation for most days, but occasionally the value goes well above the diurnal values, indicating that E_s occurred.

OBENBERGER ET AL. 4 of 17

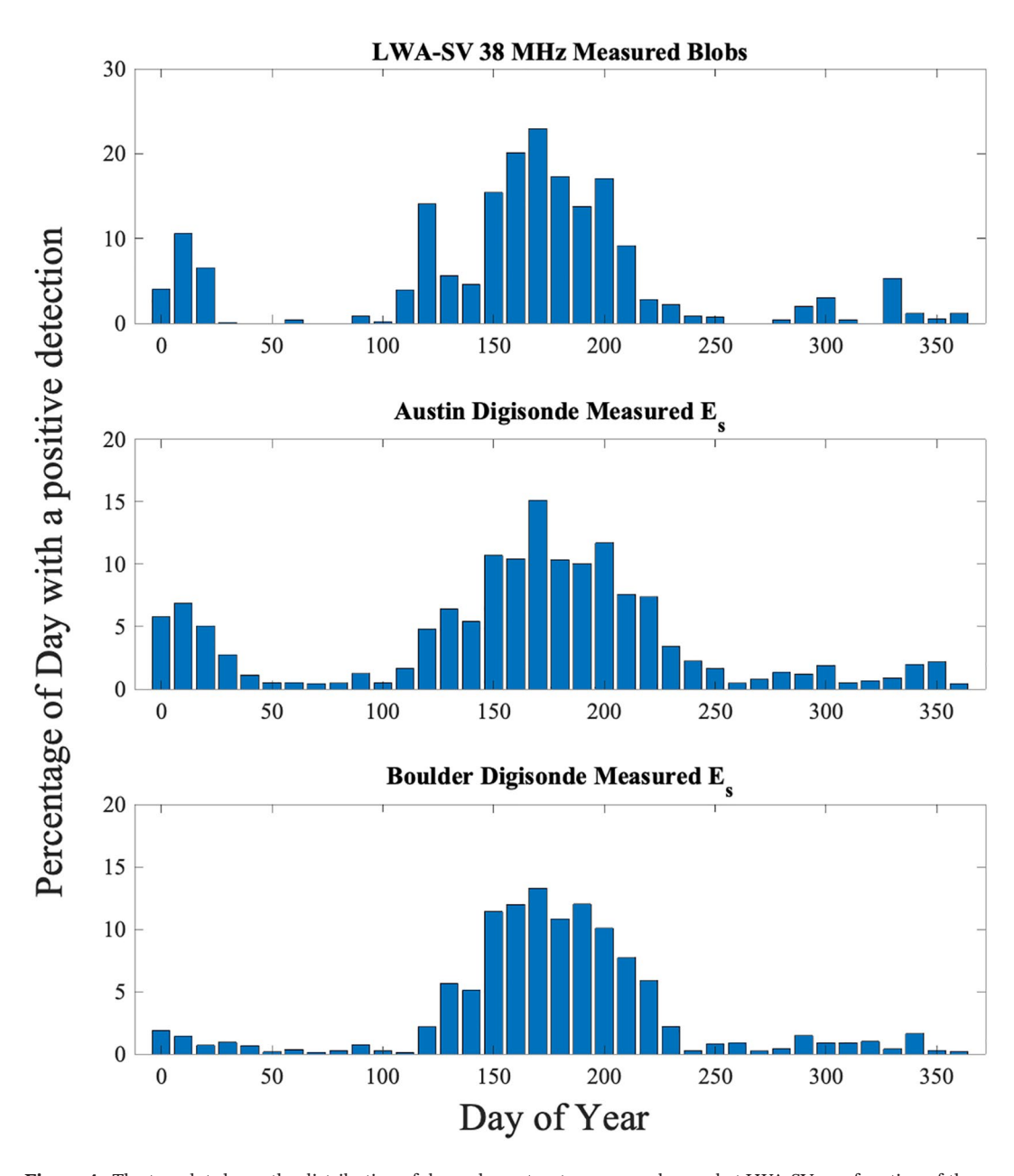


Figure 4. The top plot shows the distribution of days where structures were observed at LWA-SV as a function of the day of year. The lower two plots show the proportion of days where E_s is detected by the Austin (Middle) and Boulder (Bottom) Digisondes Each plot is averaged over a 2 years window (March 1, 2018–February 29, 2020) and are binned in 10 days averages.

The occurrence of the phenomena was recorded simply by visual inspection of LASI movie files created at the end of each day (http://www.phys.unm.edu/~lwa/lwatv2.html). We recorded the time and date when structures appeared and later disappeared. This was done using LWA-SV data between March 1, 2018 and February 29, 2020. The length of all time windows on a given day can then be used to find the percentage of time when structures are observed by LWA-SV.

Figure 4 shows the percentage of day (as a function of Day of year) where LWA-SV observed structures, and the Digisondes in Boulder and Austin observed E_s . The values for all three plots are averaged over a 2 years window (March 1, 2018–February 29, 2020) and are binned in 10 days averages. It is clear from Figure 4 that the occurrence of the structures are well-matched with the occurrence of E_s at the Boulder and Austin Di-

OBENBERGER ET AL. 5 of 17



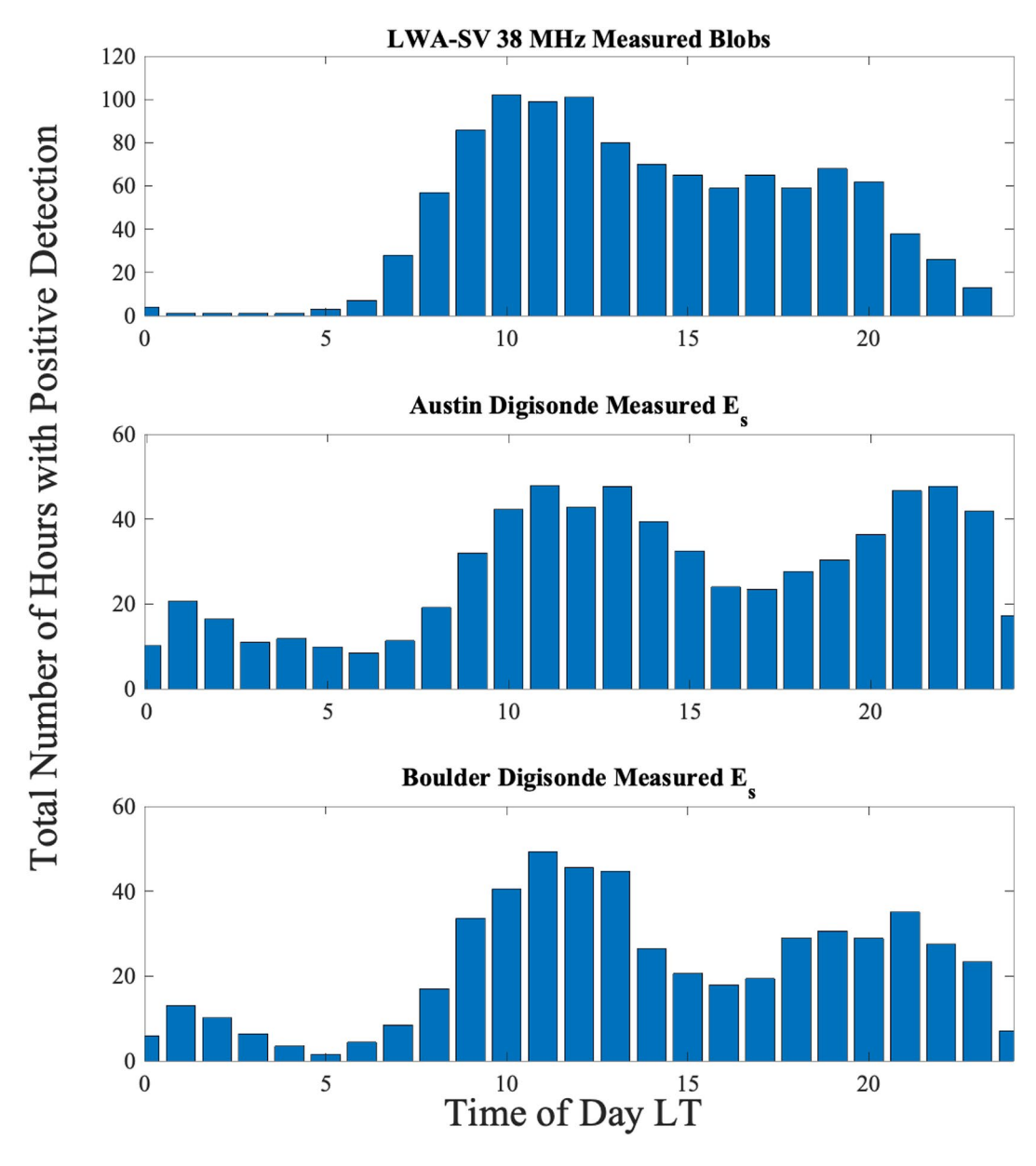


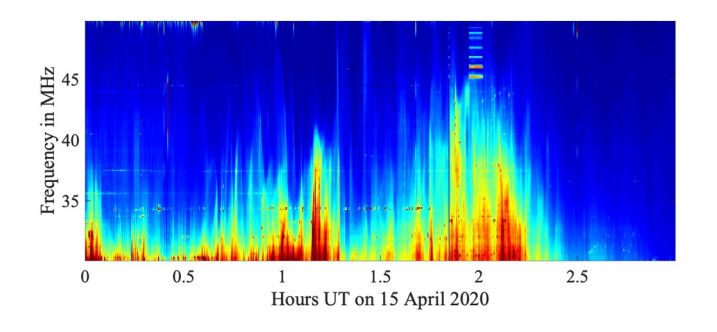
Figure 5. The top plot shows the total number of hours that structures were observed at LWA-SV as a function of the time of day (local standard time). The lower two plots show the total number of hours that E_s was detected by the Austin (Middle) and Boulder (Bottom) Digisondes as a function of time of day (local standard time). Each plot is binned in 1 h periods, and the data for each plot is taken from a 2 year window (March 1, 2018–February 29, 2020).

gisondes. A clear peak near the summer solstice (\sim day 172) exists for all three samples, and this agrees with the known climatology of midlatitude E_s (Haldoupis et al., 2007; Whitehead, 1989). The Austin Digisonde and LWA-SV observations also show a significant secondary peak in January.

Similarly, we can inspect the time of day when structures are observed from LWA-SV and compare them to the time of day when E_s is observed from each Digisonde. Figure 5 shows the total number of hours where structures were observed by LWA-SV (top) as a function of time-of-day, over the 2 hour period. Time-of-day is given in local standard time. Figure 5 also shows the total number of hours where E_s is detected by the digisondes at Austin (middle) and Boulder (bottom), as a function of time of day. All data is taken from the same 2 year period.

OBENBERGER ET AL. 6 of 17





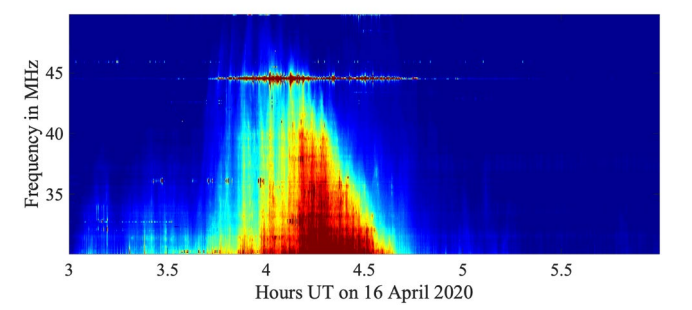


Figure 6. Dynamic spectra for structures observed near the horizon on April 15, 2020 at an azimuth of 150° (top) and April 16, 2020 at an azimuth of 117° (bottom).

As can be seen by the graphs in Figure 5, the LWA-SV structures and digisonde E_s detections occur in a similar bi-modal distribution with a peak around local noon and in the late evening. The late evening bump is less noticeable in the LWA-SV data. Moreover, the LWA-SV data shows almost no detections between midnight and 0600 LT.

The data presented in Figures 4 and 5 show that the phenomena observed by LWA has a climatology very similar to E_s observed by the Austin and Boulder digisondes. While this alone does not prove the phenomena is itself E_s , it implies an association.

3.2. Analysis: Spectral Characteristics

The broadband all-sky imager at LWA-SV allows us to produce a 20 MHz spectra on 5 s integrations for any region in an all-sky image. Analysis of the broadband all-sky images from structures on 15 and 16 April 2020, show that the spectra of the phenomenon is broad and smooth and gets brighter at low frequencies. Figure 6 shows the dynamic spectra of two bright regions on April 15 and 16, 2020.

As can be seen from this figure, the spectra are dominated by broadband emissions that vary in brightness. The spectra also contain a few narrowband emissions as well, which are indicative of scattered communications signals. The broadband emissions are also highly dynamic with clearly visible frequency/time modulations. Particularly in the 16 April data, we

can clearly see quasi-periodic temporal structure in the broadband emissions. Integrating between 40 and 44 MHz and performing a continuous wavelet transform, we can isolate the frequencies of oscillation.

Figure 7 shows the bandwidth (40–44 MHz) integrated light curve and continuous wavelet transform from the dynamic spectra from April 16, 2020. Note the excess power observed between 0.002 and 0.006 Hz, which correspond to periods of \sim 2.5–8 min. Such periods are often observed in the ionosphere and are indicative of both acoustic waves and gravity waves.

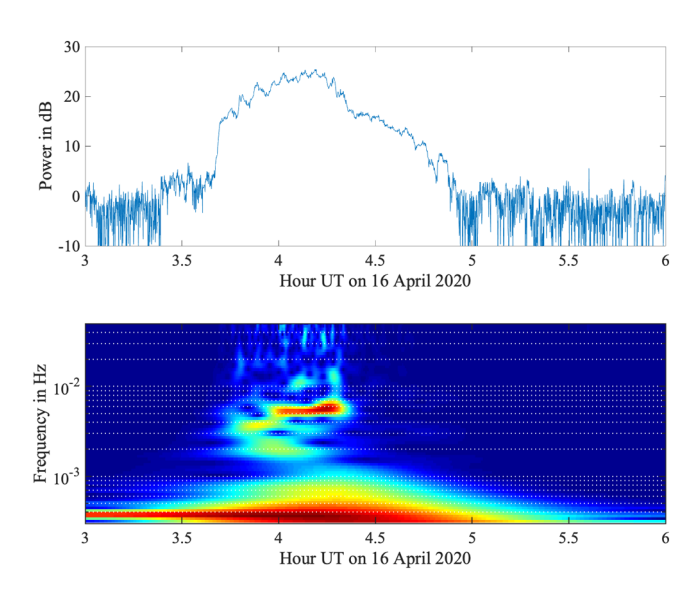


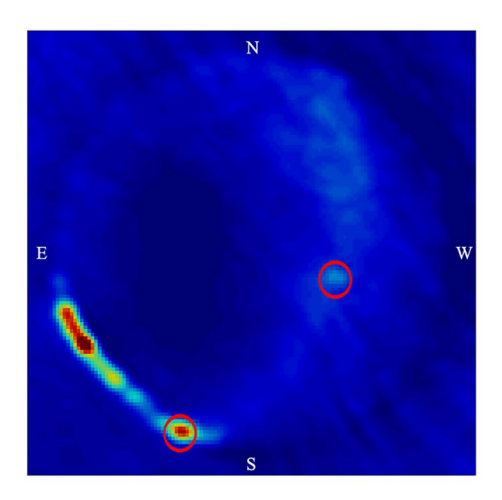
Figure 7. (Top)Light curve derived from the bandwidth integrated dynamic spectra from April 16, 2020 shown in Figure 6. (Bottom) continuous wavlet transform of the light curve shown on top. Note the excess power between 0.002 and 0.006 Hz. These frequencies correspond to periods of ~ 2.5 –8 min.

The broadband nature of the emission suggests that whatever is producing the emission is a reflection of either natural or unintentional human-made radio emissions, or combination of both. The two most likely sources include lightning (Proctor, 1981) or the burst-like noise caused by arcing power-lines and connected hardware such as transformers (Loftness, 1997; Pakala & Chartier, 1971). Both of these sources are well known to be bright and broadband.

We note that the overall shape of the dynamic spectra bears a striking resemblance to spectra reported recently by Fung et al. (2020). Here the authors describe spectra that have a "tent" like shape, where the observed emissions increase as function of frequency and then later decrease. Fung et al. (2020) discount changing properties of the ionosphere because there "is no a priori reason to favor particular phase of the changes" of their tent like structures. Yet the authors fail to consider the fact that two of their reported observations occurred during days of geomagnetic activity, during which the ionosphere is highly dynamic, even at midlatitudes. Moreover, the authors ignore propagation paths created by E_s , which would follow a rapid increase and later decrease in plasma frequency, creating propagation paths for distant radio emissions. However, without a statistical study of the occurrence of their spectral features it is impossible to make a full comparison. Based on an occasional appearance of burst-like emission, Fung et al. (2020) also claim that RF emission is most likely coming from

OBENBERGER ET AL. 7 of 17





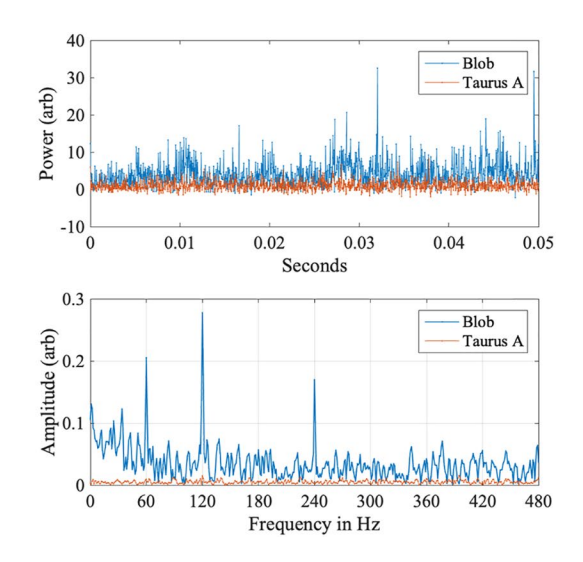


Figure 8. (Left) An example all-sky image from LWA-SV showing traveling structures to the SE. (Top Right) High time resolution ($40 \mu s$) light curve of bright structure within red circle to the SE shown on image and comparison light curve of radio source Taurus A marked by red circle to the W. (Bottom Right) Power spectra of light curves for both bright structure within red circle to the SE and Taurus A. Note the strong 60, 120, and 240 Hz signal in the power spectra of structure.

distant lightning storms, and provide a geometrical argument for this. However, it is difficult to judge the validity of this hypothesis given the lack of comparison to actual lightning data, which is readily available.

3.3. Analysis: Temporal Characteristics

From the LASI images, it is evident that the brightness of the structures most often varies slowly with time. This indicates that distant lightning is not a common cause, as lightning creates irregular burst-like radio emission in the HF and VHF bands. However, on the five second time scales of LASI images, unintentional human-made noise coming from power-lines would appear to vary slowly. Power-line noise is composed of many sources of broadband bursts repeating at 60 Hz, but the brightness averaged over 5 s changes little (Loftness, 1997; Pakala & Chartier, 1971).

To test the human-made hypothesis, we needed high time resolution data to be able to resolve the telltale signature of power line noise, namely bursts repeating at 60 Hz (and/or its harmonics). To image at such a high cadence, we would need to record raw voltage data from each antenna.

Since the phenomena are transient and difficult to predict, scheduled recordings of the raw data are impractical, and at a data rate of 357 GB/hr, continuous recording is impossible. Rather we regularly checked LWATV and waited diligently for the phenomenon to appear. On 19 June 2019 at \sim 1500 UT (9 a.m. LT) structures appeared in the SE of each LWA station. The structures grew in size and brightness and at \sim 2000 UT (1400 LT), we triggered a recording of the raw data from LWA-SV with a center frequency of 38 MHz. Using a similar technique as LASI, we used the raw data to produce all-sky images with a time resolution of 40 μ s.

Analyzing the pixels associated with the structures, we find that at least some of their flux is produced by short (>40 μ s) bursts, some of which repeat at a cadence of 16.6667 ms (i.e. 60 Hz). This suggests that at least some of the RF emission is coming from distant power-lines. Figure 8 shows an example all-sky image from the June 19, 2019 event, as well as a 40 μ s resolution light curve and a power spectrum from a bright structure to the south highlighted with a red circle. For comparison, a light curve and power spectra is shown for Taurus A, a supernova remnant located with a red circle to the W. No 60 Hz component is seen for Taurus A, suggesting that the 60 Hz seen from the structure is not an artifact.

Follow-up observations were carried out on September 9, 2019 at 18 UT, when LWATV showed structures in the NE for both stations. This time we recorded raw data from both stations to make sure the 60 Hz com-

OBENBERGER ET AL. 8 of 17

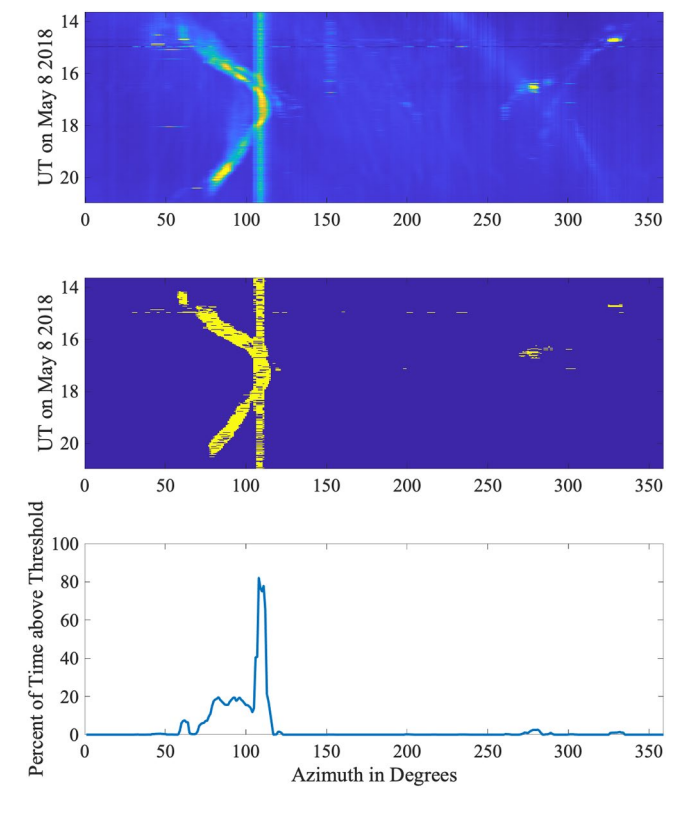


Figure 9. (Top) Plot of relative power as a function of time and Azimuth angle for sources near the horizon at elevation angles between 0° and 15°. (Middle) Binary threshold mask of the top plot, where the threshold value is chosen such that setting astrophysical sources are not counted. (Bottom) A plot showing the percent of time that a given azimuth contains power above the threshold. This is calculated simply by summing the mask across the time axis and multiplying by 100. Note in all three plots the persistent local power-line noise near 110°.

ponent was not just a feature seen in a single station. Similar to the data described above, these data showed the existence of a burst component occurring at 60 Hz, which accounts for at least a part of the total emission. Since power-lines known to produce arcing are widespread, it is certainly possible that specular conditions could be met for many locations from a single structure.

3.4. Analysis: Azimuthal Distribution

If the emissions were indeed originating from faulty power-line hardware, then the emissions would likely be brightest in metropolitan centers. These emissions could reach the LWA stations from a variety of geometries, but for the case of a specular ionospheric reflection from plasma distributed parellel to Earth's surface, the azimuthal distribution measured from the LWA would point toward the direction of initial radiation. For the case where the emissions scatter from FAIs in the ionosphere, the azimuthal distribution would point to the direction where the incident ray, scattered ray and normal to the geomagnetic field are all in the same plane. These typically appear as arcs of emission across the sky (Helmboldt & Taylor, 2020), a feature not associated with the structures reported in this paper.

Over the 2 years span used for this study, the vast majority of the observed structures were located near the horizon, and for specular type reflections, we would expect more reflections at lower elevation angles for two reasons. First, there is more observable ionosphere at lower elevation angles, meaning that there are more potential sources of reflection. Second, while for vertical incidence reflections the emission needs to be below the critical frequency (f_c ; maximum plasma frequency of the ionosphere), away from zenith lower frequencies are usable. The maximum usable frequency (MUF) is related to the critical frequency by

$$MUF = f_c \times sec(\theta), \tag{1}$$

where θ is the angle of incidence. For distances where the flat earth approximation can be used, the angle of incidence is nearly equal to the zenith angle (90° - the elevation angle). From Equation 1, it is clear to see that near the horizon typical value for fo E_s , could often enable reflections up at LWA operating frequencies.

Since most structures occur near the horizon, we can estimate the azimuthal distribution by analyzing the pixel values near the horizon for each time window when structures where observed. The top plot of Figure 9 shows the relative power on the horizon as a function of azimuth and time for structures that were observed from \sim 14 to 21 UT on May 8, 2018. As can be seen from this plot, the structures appeared near an azimuth of 50° and drifted to around 120° after which the same set or a different set then drift back to 50°. Meanwhile, structures also appeared at 280° and 330°. Note the persistent signal at 110°, which is associated with emissions from local power-lines only a few km away from LWA-SV. These power-lines block observations in that direction, and for this reason the temporal analysis above that shows the 60 Hz signal does not use the directions associated with local power-lines.

We can apply a brightness threshold as a means of identifying when and at what azimuth structures are occurring. The middle plot of Figure 9 shows a threshold image, where values above the threshold are given the value one (shown in yellow) and values below the threshold are given the value zero (shown in blue). The bottom plot shows the average of all threshold pixels at each azimuth, thereby providing the percent of time a given azimuth is above the threshold. The threshold value was chosen to be greater than the brightest setting astrophysical source, such that astrophysical sources would not contaminate the processing.

As Figure 4 shows, many cases of structure activity occur in late summer, which is monsoon season in the southwest United States. Therefore, the pixels on the horizon will often be contaminated by local lightning.

OBENBERGER ET AL. 9 of 17



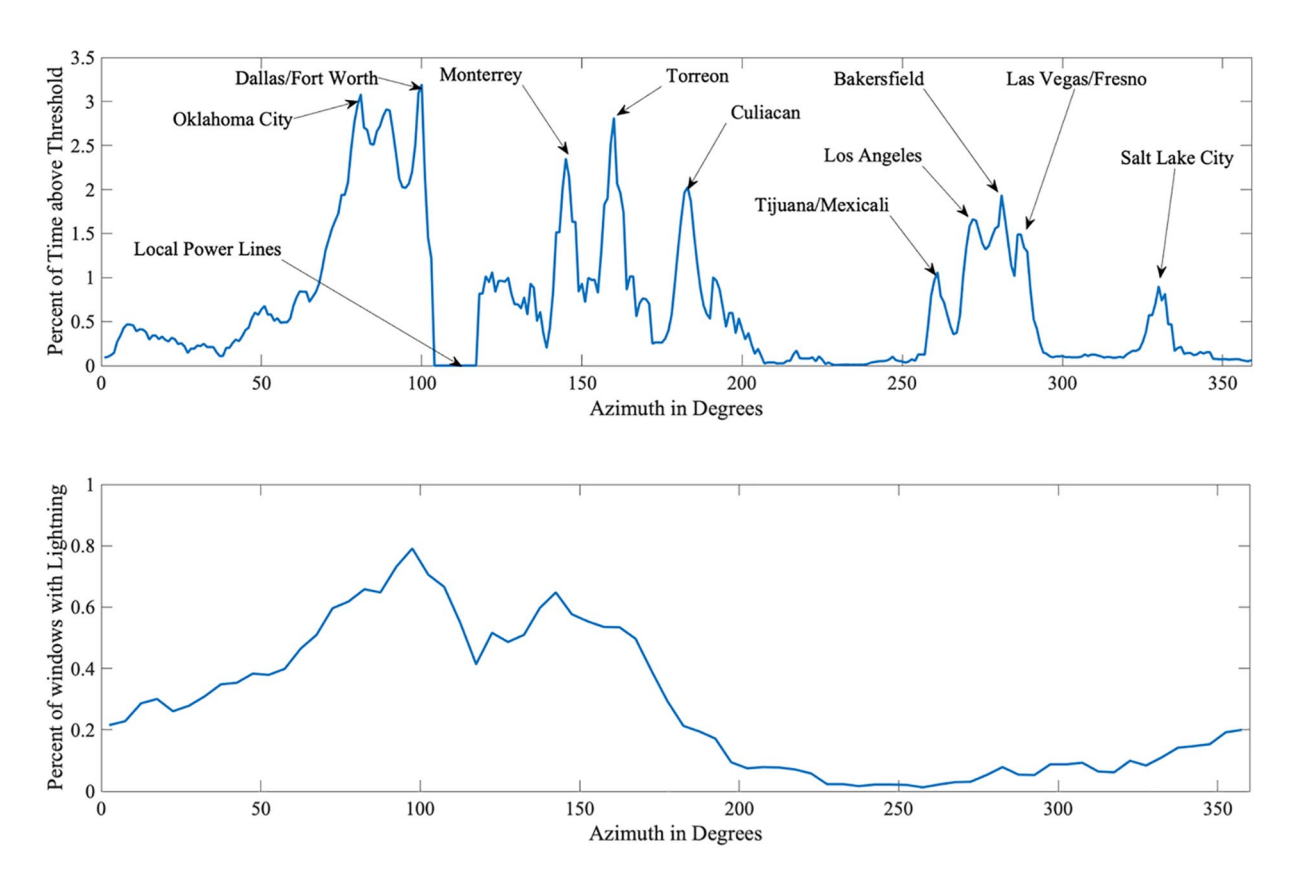


Figure 10. (Top) Plot shows the azimuthal distribution for the total percent of time above the chosen threshold for sources on the horizon. We have labeled a number of identifiable peaks which correlate well with large metropolitan areas that fall within an annulus with inner and outer radii of 700 and 1,250 km radial respectively. We also note the area around 110° where we have masked out the signal due to strong emissions from power-lines local to LWA-SV. (Bottom) Plot shows the azimuthal distribution of GOES/GLM measured lightning at ranges between 500 and 2,500 km from LWA-SV during for 1 h windows when the structures were observed.

Since the targeted structure activity is relatively smooth over time, we can exclude local lightning by removing pixels that are "delta-function-like" in time. This is accomplished by using time differencing to identify spikes in power, which we then mask out using a threshold.

Once the effects of local lightning are removed, we can then compute the average azimuthal distribution over the entire 2 years period. Figure 10 shows the averaged distribution, and Figure 11 shows this average extended in an annulus with an inner and outer radius of 700 and 1,250 km, respectively. These radii correspond to specular reflections, off plasma distributed parallel to Earth's surface, at elevation angles between 15° and 5° respectively for an altitude of 100 km. The annulus is then plotted on top of a night-time view of earth where population centers are identified by city lights. From this figure, it is easy to see that the azimuthal distribution correlates well with large population centers in a radial distance range between 700 and 1,250 km. Figure 10 identifies several likely cities in both the United States and Mexico. Note the local power-lines, which happen to be in the direction of Austin and Houston, TX have been masked out in Figures 10 and 11. Figure 12 shows a similar image but uses data from LWA1 over the same two year period. As can be seen the Azimuthal distribution is quite similar, pointing to the same cities as LWA-SV.

The fact that the azimuthal direction points toward an origin indicates that the process is a mirror-like reflection from an overdense plasma layer parallel with the surface of the earth. This distribution also rules out the possibility of scatter from FAIs because the angle of scatter from FAIs must be equal to the angle of incidence with respect to the geomagnetic field. The scattered rays form a cone that contains the extension of the incident ray beyond the FAIs and with the geomagnetic field at the scatter point forming the axis of symmetry, similar to how light scatters from a reflective rod (Barry, 1974; Stathacopoulos & Barry, 1974). This can be

OBENBERGER ET AL. 10 of 17

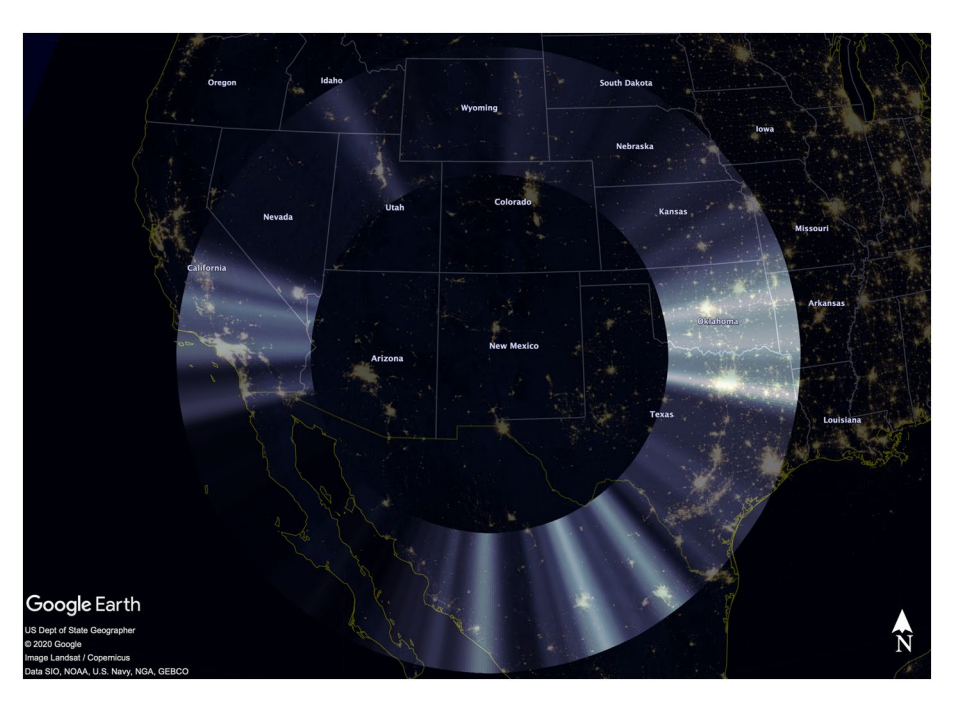


Figure 11. Satellite imagery of the nighttime earth, highlighting population centers which are observable by their visible light output. The image is provided by the NASA Black Marble project and mapped using Google Earth Pro. The image is centered over New Mexico with the surrounding areas of the United States and Mexico, and is overlaid with the relative azimuthal distribution of the structures observed near the horizon, at 38 MHz by LWA-SV. The structures most often appear in directions that intersect large metropolitan areas in the US and Mexico at radii between 700 and 1,250 km from LWA-SV.

expressed analytically by the expression $\hat{\mathbf{k}}_i \cdot \hat{\mathbf{B}} = \hat{\mathbf{k}}_r \cdot \hat{\mathbf{B}}$ where $\hat{\mathbf{k}}_i$ and $\hat{\mathbf{k}}_r$ are unit vectors in the direction of the incident and scattered rays, respectively, and $\hat{\mathbf{B}}$ is the unit vector in the direction of the geomagnetic field at the scatter point (D. L. Hysell & Chau, 2001). Consequently, at mid-latitudes in the Northern Hemisphere,



 $\textbf{Figure 12.} \ \ \text{Same image as Figure 11} \ \ \text{but uses LWA1 data instead of LWA-SV.}$

OBENBERGER ET AL. 11 of 17



signals received at low elevation angles from the south cannot result from FAI scatter unless the original signal sources are located at high altitudes or in space.

To acquire limits on azimuths of low-elevation signals received that are possible by FAI scatter, we calculated the angle of incidence for signals observed at LWA-SV assuming those signals were scattered from ionosphere plasma structures aligned with the geomagnetic field. Stepping through azimuth in 5° increments, at elevation angles of 0°, 5°, 10°, and 15°, and altitudes from 90 to 250 km with 20 km increments, we calculated which arrival vectors satisfy $\left| (\hat{k}_i - \hat{k}_r) \cdot \hat{B} \right| \le \epsilon$ such that a corresponding incident vector exists originating from the ground. The magnetic field direction was provided by the International Geomagnetic Reference Field and the threshold ϵ was chosen to be 0.10 to allow for scatter from irregularities that are not exactly field aligned. We find no incidence angles pointing back to the surface of Earth for azimuths between 110° and 260°. Clearly from the azimuthal distribution shown in Figure 10 where many sources appear in this azimuthal range, discounts scatter from FAI completely.

3.5. Analysis: Comparison to Lightning

We note that by removing local lightning, we would also be removing non-local lightning, where the distant lightning emissions could be reflecting off of the same E_s structures or as Fung et al. (2020) suggest, the F region. Certainly if we are able to observe the RF noise from a distant city, then distant lightning may also be observable.

We also note that while 60 Hz is easily identified in the high time resolution imaging, it may not account for all of the emissions. Similar to power-line noise, it is possible that with a high enough rate of lightning, a distant storm could appear unresolved in time by the LASI images, which are integrated for 5 s each. For a maximum reflection altitude of 200 km (F region), we estimate that the maximum range of a potential source is \sim 2,500 km.

A simple test can be carried out to identify if radio emission from lightning could be a common cause. Lightning data are readily available from the Global Lightning Mapper (GLM) on board the Geostationary Operational Environmental Satellite-16 (GOES-16) which observes North America and Central America. We can simply compare the azimuths and times of observed structures to the azimuthal directions and times to GLM lightning events. For this test, we sum the GLM detected lightning events occurring at ranges between 500 and 2,500 km and bin the events into 5° chunks within 1 h intervals. If at least one lightning event occurred in an azimuthal bin within that hour, we classify that bin as having a potential source of lightning radio emissions. We then compare this azimuthal occurrence from each hour to the azimuthal distribution of observed structures for that hour, using the same threshold given in Section 3.4 but without removing lightning-like bursts. If an azimuthal bin for a given hour has both at least one lightning event, and an observed structure we classify that bin as a potential ionospheric reflection of lightning.

Using this method, we find that 32% of detected structures are azimuthally and temporally coincident with lightning at ranges between 500 and 2,500 km. Similarly, we find that 25% of lightning is azimuthally and temporally coincident with observed structures. However, on average 20% of bins in a 1 h window contained lightning and 16% contained structures. Meaning that if we assume random distributions of both lightning and observed structures, there is a 20% chance a given structure will line up with a lightning event and a 16% chance lightning will line up with observed structures. This small amount of excess above random chance could be evidence that some of the observed structures are indeed caused by reflected RF from lightning. However, this small amount of additional correlation may be dominated by the fact that most of the lightning in this range occurs to the South East of New Mexico, where there is also a large number of metropolitan centers.

Figure 10 shows both the azimuthal distribution of the structures, as well as the azimuthal distribution of lightning as seen from LWA-SV. As can be seen in this figure, most of the lightning occurs at azimuthal angles between 50° and 170°. This region also shows an increase in the azimuthal distribution of the observed structures, but it also has a larger number of metropolitan centers (see Figures 11 and 12). Furthermore, since almost no lightning is detected in between 200° and 300°, we can say for certain that lightning cannot be a source of emission in those directions. From this data, it is difficult to determine exactly how much

OBENBERGER ET AL. 12 of 17



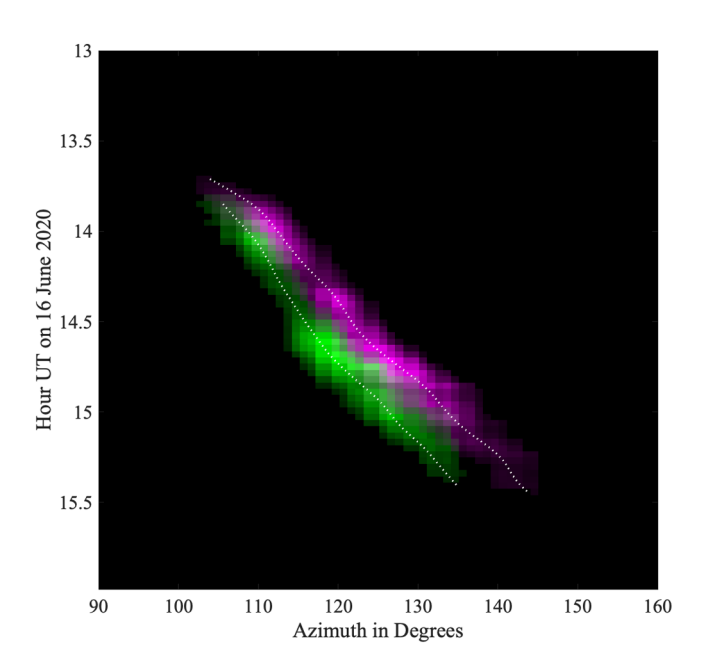


Figure 13. A plot showing relative power as a function of Time (UT) and the Azimuthal angle for both LWA1 (Green) and LWA-SV (Magenta). Both stations see the same structure on June 16, 2019 in different azimuthal directions as it drifts, allowing for an estimate of the distance and speed. The smoothing spline fits of the measured azimuths are overlaid for each station.

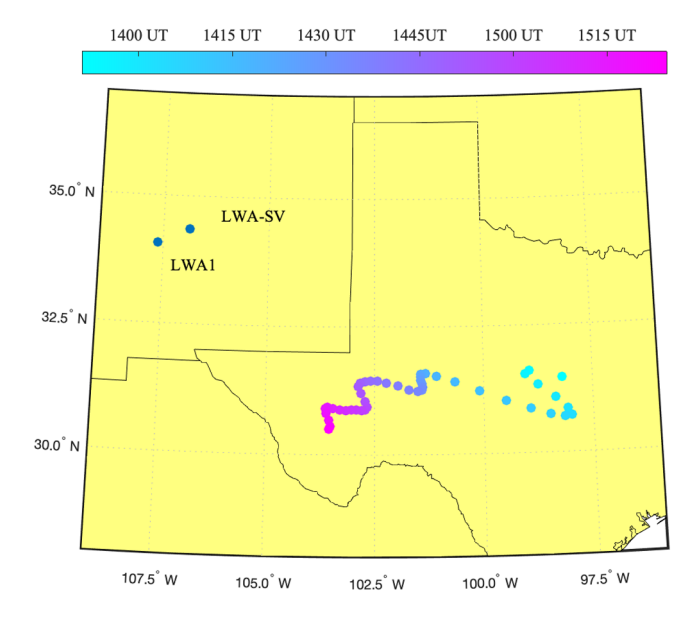


Figure 14. A map showing the estimated position of the E_s structure is shown in Figure 13. The color bar indicates observing time. The structure clearly moves to the southwest over the course of 1.25 h. We note the wave-like movements are consistent with azimuthal variations shared by both stations as seen in Figure 13, this implies that it could indeed be a real modulation, caused by a sources such as an atmospheric gravity wave.

lightning generated RF contributes to the observed emission. However, we can say that it likely plays only a small role if any, and that unintentional human-made emission from cities likely dominates.

3.6. Analysis: Spatial Calibration and Morphology

Figures 10–12 show that the brightest emission most often occurs in the direction of large cities. However, the emission is not limited to large metropolitan centers. Dimmer, yet still observable structures often appear in directions associated with rural areas. Apparently, vast regions have enough population to create a continuous source of illumination for E_s . Figure 9 shows the track of what appears to be two or more moving patches of E_s , that start at an azimuth of \sim 60° turn around at \sim 120° and then head back to \sim 75°. Obviously, the cities are not moving, so this represents movement of E_s structures. It is then not surprising that a traveling structure can be viewed from multiple vantage points, and this is very often the case when comparing LWA1 and LWA-SV.

Figure 13 shows a plot of relative power as a function of time and azimuth for a structure observed on June 16, 2019. The figure shows the view from both LWA1 (Green) and LWA-SV (Magenta). As can be seen from this plot both stations see what appears to be a single structure drifting to higher azimuthal angles.

Since the projection onto the sky of an all-sky image compresses at the horizon, we cannot determine an accurate elevation angle for the structures in Figure 13 as they are located near the edge of the image. However, if we assume a spherical Earth we can simply compute the intersect of two bearings (azimuths) using simple geometry. Assuming a single peak, we fit a smoothing spline to the peak pixel in azimuth as a function of time for each of the structures in Figure 13. We then compute the intersection point of these two sets of azimuths as a function of time. Figure 14 is a map showing the projected path of the triangulated Es structure as it moves over west Texas. We note the apparent wave-like structure of the path, which appears to have a wavelength on the order of 100 km and 20 min period, both consistent with an atmospheric gravity wave. The wave-like structure does not appear to be an artifact of the smoothing spline fit as it shows up in the azimuthal measurements from both stations (see Figure 13). We also note that before 1430 UT, the structure's location is such that the angular separation between of the two measurements make for poor triangulation, and may not be very accurate. Fitting a straight line to the points after 1430 UT, we estimate the structure is moving to the southwest at ~ 70 m/s.

This analysis only provides the latitude and longitude of the observed structure, and having no knowledge of either the elevation angle or the altitude does contribute slightly to the error in the two dimensional position. However, since the radius of the earth is much larger than both the height of the E region (\sim 90–150 km) and the distance to observed sporadic E (\sim 250–650 km), the approximate error in Latitude and Longitude dominated by the positioning error of the LWA telescopes, which is on the order of a degree or so. Whereas the maximum error in azimuthal angle caused by even a 100 km error in altitude is on the order of 8 arc-seconds for the observational range of the two LWA stations.

OBENBERGER ET AL. 13 of 17



Since no elevation angle information is available, the exact altitude of the E_s layer can only be guessed. However, there are some cases where the structures appear at a high enough elevation angle that no assumptions about altitude need to be made, rather they can simply be calculated through three-dimensional triangulation. One such event occurred on June 20, 2019 beginning at ~1700 UT (11 a.m. LT), where structures appeared at an elevation angle of roughly 50° in both stations. The structures then travel to the SW, disappear after a few minutes, and then reappear further to the SW a few minutes later. While the structures are observable for a few hours, after about 30 min they are too low in elevation angle to get accurate positional measurements.

Initially, each station sees a single structure, and triangulating the centroids, as measured by each station, results in a location of 33.64° N, 106.39° W, and 115 km altitude, which is in the E region of the ionosphere. The error contributed by the LWA synthesized beam pattern alone is ± 15 km in all directions. We note that the triangulation assumes that the reflecting region is illuminated from different sources, and it is small enough that both stations are observing plasma in the same geographic region. Assuming a perfect mirror-like reflection, the observed emission is estimated to originate in the area around Alamogordo, NM.

The right half of Figure 15 shows the structures on June 20, 2019 from each station, projected onto a geographic coordinate system, for five consecutive snapshots separated by 150 s starting 1,200 s after the structures first appear. It is clear in these images that the structures are aligned along a front oriented NW-SE and propagate from the NE. A white dashed line is plotted over the first LWA-SV image as a visual guide to see the front orientation. A corresponding all-sky movie from each station is included in the supporting information.

On January 12, 2019 beginning at \sim 1800 LT, another group of structures was observed moving S, with the highest structure being seen at \sim 30° at both stations. Triangulating the position to this structure, we find a position above SE New Mexico, at a latitude, longitude, and elevation of 32.92°N, 106.71°W, and 115 km respectively. The structures move to the S, where they disappear after a few hours. The left half of Figure 15 shows five consecutive, 150 s snapshots of these structures as they propagate from the N. These images clearly show that the structures are aligned in a W-E oriented front. A white dashed line is plotted over the first LWA-SV image as a visual guide to see the front orientation.

It is difficult to estimate a velocity of a single structure, as the brightness of each varies to the point of disappearing and reappearing. Rather we can estimate a speed of the front by converting to a one dimensional problem. We first transform the images in Figure 15 to the Cartesian East North Up coordinate system, and then rotate the E and N coordinates to account for the apparent orientation of the front, which is measured by eye. For the 20 June 2019 event, we estimate the front is perpendicular to an azimuth of 30° in LWA-SV and 25° in LWA1. Rotating the coordinates such that the front travels along one dimension, we can calculate the difference in position at each integration. Tracking the average positional change, we estimate the front is traveling at 94 ± 36 m/s. Repeating this analysis for the January 12, 2019 event, we estimate the front is perpendicular to an azimuth of 0° and is traveling at a speed of 76 ± 37 m/s.

4. Discussion and Conclusions

We have presented LWA observations of traveling structures that are characterized by broadband radio emission in the upper HF and lower VHF bands. The structures occur with a similar climatology to E_s , as measured by local Digisondes. Analysis of the azimuthal distribution indicate that much of the emission originates in large metropolitan areas that are 700–1,250 km distant from each LWA station. Moreover, the emission contains spark-like bursts of broadband emission repeating at 60 Hz, which further points to unintentional noise from caused by human-made devices attached to the 60 Hz AC power grid. We show that radio emission from lightning, likely plays only a small role (if any) in the overall observed emissions.

The fact that the azimuthal distribution points to the location of origin implies that the scattering processes is mirror-like, where the emission undergoes a specular reflection off plasma distributed approximately parallel to Earth's surface. The association with E_s suggests that dense E_s structures are reflecting unintentional, broadband emissions from human-made devices back to the ground. Such a process is consistent with the fact that the structures are almost always observed on the horizon, where the MUF can be much higher than the maximum plasma frequency of the observed E_s layer. While most observations are centered at 38 MHz,

OBENBERGER ET AL. 14 of 17



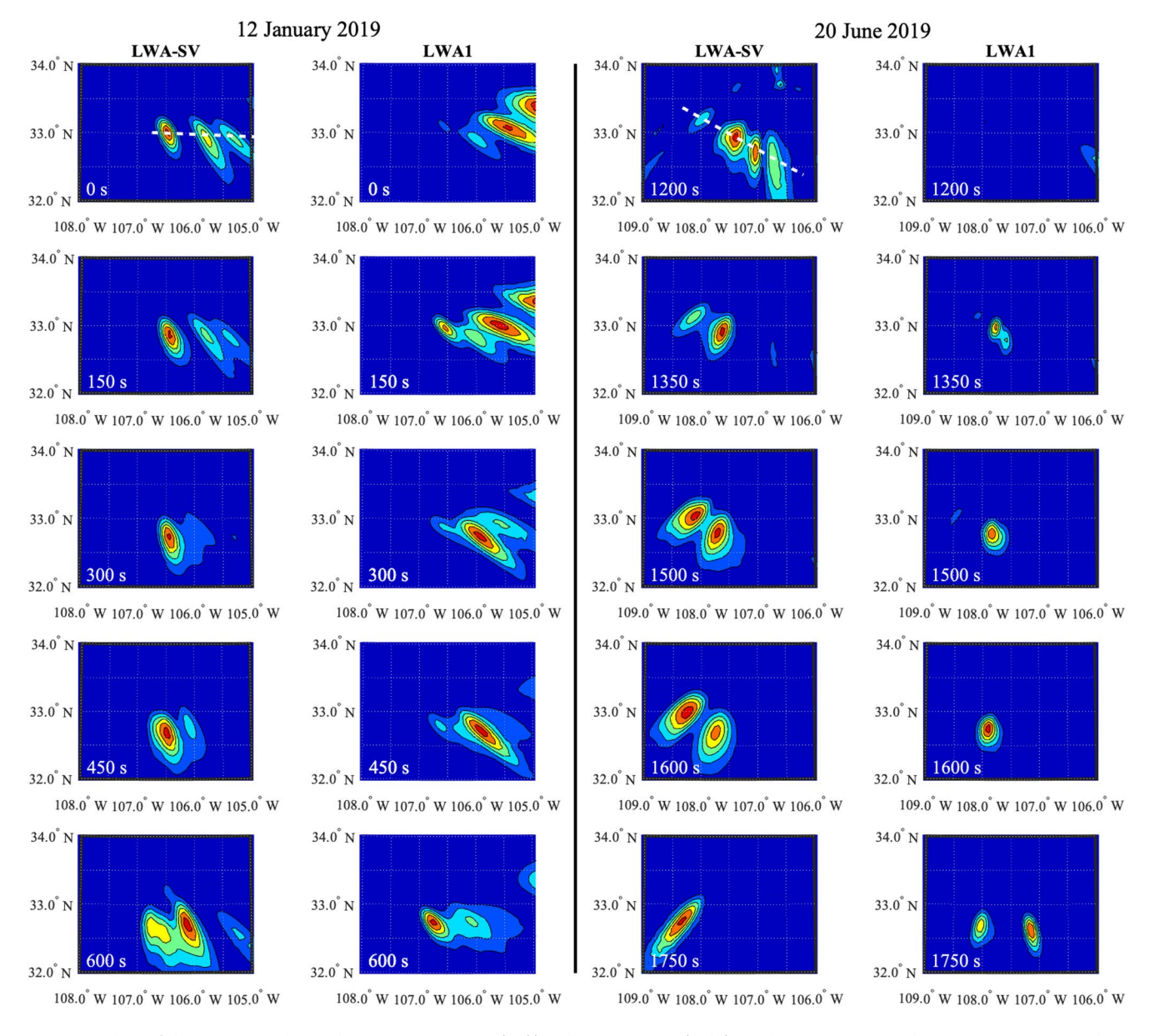


Figure 15. Snapshots of the structures observed on January 12, 2019 (Left) and June 20, 2019 (right). Each image is projected onto a geographic coordinate system assuming a height of 115 km and is normalized to the brightest point. For the January event, the structures are shown starting from the time they first appear, but for the June event the structures are shown starting at 1,200 s after they appear to highlight their arrangement in a front. A white dashed line is plotted over the first LWA-SV image for each day as a visual guide to see the front orientation. Note: structures appear bigger and more elongated at later times due to the projection of the image at lower elevation angles.

the low elevation angles involved imply a plasma frequency well below this. However, at times the elevation angles are high enough to imply that the plasma frequency of E_s can reach into the VHF band. One such case occurred on June 20, 2019, where the structures were seen at an elevation angle of nearly ~50°.

For cases where an elevation angle can be determined, the dynamic spectra will likely enable an estimate of foE_s . Here we can assume the upper frequency cutoff of the emission is the MUF, and using Equation 1 we can then then calculate foE_s . Such an estimate may be highly valuable for models of E_s , where our technique could enable measurements of foE_s over vast regions of the ionosphere.

As described in Section 3.6, the two LWA stations can be used in tandem to triangulate E_s structures. This is easiest when the structures are at high elevation angles and the triangulation is trivial, but in most cases

OBENBERGER ET AL. 15 of 17



the structures are seen at the horizon, where only the azimuthal angle can be measured. In such cases the latitude and longitude can be measured, but the altitude is missed. For such measurements, any estimation of the electron density would need to rely on guessing the altitude of the E_s layer. However, in the future this could be remedied by adding broadband capabilities to LWA1 or future LWA stations. With the Latitude and Longitude solved by the Azimuths, the MUF measured by two or more stations could be used to solve for the altitude and electron density through an optimization of Equation 1. Here the zenith angle could be replaced with the geometric relationship between the ground distance and the altitude.

The structures reported in this paper appear in propagating fronts traveling at 50–100 m/s, a feature that is consistent with other observations of E_s discussed in Section 1. We note that while GPS networks and coherent scatter radars have been able to map and track E_s fronts, they do not provide information about the actual plasma frequencies involved. Our technique may indeed provide this information, where the images provide the spatial structure of the fronts, and the spectra could provide the upper plasma frequency cutoff.

Future all-sky imaging observations using the full 20 MHz bandwidth capability of LWA-SV may allow for spatially resolved measurements of electron density within the structures. However, we note that this presumably could only be done using continuous emission sources such as large metropolitan areas. Indeed, the movie provided in the supporting information shows that LWA1 and LWA-SV do not see exactly the same structural information. Rather, they only observe the structure that is made visible by the geometry of sources on the ground. Therefore, it can be assumed that for at least the rural areas of New Mexico, which are sparsely populated, there is not enough emission to fully sample the small scale structure. This is also true for vast regions of Baja California, Nevada, and Wyoming, which as Figures 11 and 12 show, do not have enough population density to reliably enable E_{s} detection.

In Sections 3.2 and 3.6, we presented observations that contained quasi-periodic amplitude and spatial modulations with frequencies consistent with atmospheric gravity waves and acoustic waves. Statistical studies of these signatures may be valuable for determining the relationship between gravity waves and E_s formation.

Data Availability Statement

All of the LASI data used in this article are publicly available at the LWA Data Archive (http://lda10g.alliance.unm.edu), other data can be provided upon request. All of the GIRO data used in this article are publicly available at http://giro.uml.edu. The authors acknowledge the use of GOES GLM data, which is provided by NOAA and can be accessed at https://www.avl.class.noaa.gov.

Acknowledgments

The authors thank the anonymous referees for their insightful comments and suggestions, Special thanks to J. Vincent Eccles (SDL), Eugene Dao (AFRL), Todd Parris (AFRL), and Joe Helmboldt (NRL) for highly instructive conversations. This research was funded in part by the Air Force Office of Scientific Research (AFOSR). Construction of the LWA has been supported by the Office of Naval Research under Contract N00014-07-C-0147 and by the AFOSR. Support for operations and continuing development of the LWA1 is provided by the Air Force Research Laboratory and the National Science Foundation under grants AST-1835400 and AGS-1708855.

References

Barry, G. H. (1974). HF-VHF communications experiment using man-made field-aligned ionospheric scatterers. *Radio Science*, 9(11), 1025–1032. https://doi.org/10.1029/RS009i011p01025

Bernhardt, P. A. (2002). The modulation of Sporadic-E layers by Kelvin-Helmholtz billows in the neutral atmosphere. *Journal of Atmospheric and Solar: Terrestrial Physics*, 64, 1487–1504.

Chu, Y. H., & Wang, C. Y. (1997). Interferometry observation os 3-dimensional spatial structures of sporadic E using the Chung-Li VHF radar. *Radio Science*, 32, 817–832.

Cosgrove, R. B., & Tsunoda, R. T. (2002). A direction-dependent instability of Sporadic-E layers in the nighttime midlatitude ionosphere. Geophysical Research Letters, 29, 1864.

Cosgrove, R. B., & Tsunoda, R. T. (2004). Instability of the E-F coupled nighttime midlatitude ionopshere. *Journal of Geophysical Research*, 109, A04305, https://doi.org/10.1029/2003JA010243

Cranmer, M. D., Barsdell, B. R., Price, D. C., et al. (2017). Journal of ASTM International, 6(4), 1750007.

Didebulidze, G. G., & Lomidze, L. N. (2010). Double atmospheric gravity wave frequency oscillations of sporadic E formed in a horizontal shear flow. *Physics Letters A*, 374, 7.

Ellingson, S. W., Taylor, G. B., Craig, J., Hartman, J., Dowell, J., Wolfe, C. N., et al. (2013). The LWA1 radio telescope. *IEEE Transactions on Antennas and Propagation*, 61(5), 2540–2549.

Fung, S. F., Typinski, D., Flagg, R., Ashcraft, T., Greenman, W., Higgins, C., et al. 2020. Propagation teepee: A possible high-frequency (15-30 MHz) remote lightning signature identified by citizen scientists. *Geophysical Research Letters*, 47(11), e2020GL087307. https://doi.org/10.1029/2020GL087307

Haldoupis, C. (2012). Midlatitude sporadic E. A typical paradigm of atmosphere-ionosphere coupling. Space Science Reviews, 168, 441–461.
 Haldoupis, C., Pancheva, D., Singer, W., Meek, C., & MacDougall, J. (2007). An explanation for the seasonal dependence of midlatitude sporadic E layers. Journal of Geophysical Research, 112, A06315. https://doi.org/10.1029/2007JA012322

Helmboldt, J. F. (2016). A multi-platform investigation of midlatitude sporadic E and its ties to E-F coupling and meteor activity. *Annales Geophysicae*, 34(5), 529–541.

OBENBERGER ET AL. 16 of 17



- Helmboldt, J. F., Ellingson, S. W., Hartman, J. M., et al. (2014). All-sky imaging of meteor trails at 55.25 MHz with the first station of the long wavelength array. *Radio Science*, 49(3), 157–180. https://doi.org/10.1002/2013RS005220
- Helmboldt, J. F., & Taylor, G. B. (2020). All-sky tracking of sporadic E field-aligned irregularities as a novel probe of thermospheric winds. Earth and Space Science, 7, 4.
- Hysell, D. L., & Burcham, J. D. (2000). The 30 MHz radar interferometer studies of midlatitude E Region Irregularities. *Journal of Geophysical Research*, 105, 12797–12812.
- Hysell, D. L., & Chau, J. L. (2001). Inferring E region electron density profiles at Jicamarca from Faraday rotation of coherent scatter. *Journal of Geophysical Research*, 106(A12), 30371–30380. https://doi.org/10.1029/2000JA001101
- Hysell, D. L., Larsen, M. F., & Zhou, Q. H. (2004). Common volume coherent and incoherent scatter radar observations of mid-latitude sporadic E-layers and QP echoes. Annals of Geophysics, 22, 3277–3290.
- Hysell, D. L., Yokoyama, T., Nossa, E., Hedden, R. B., Larsen, Munro, J., et al. (2010). Radar and optical observations of irregular midlatitude sporadic E layers beneath MSTIDs. Aeronomy of the Earth's atmosphere and ionosphere, IAGA special Sopron book series. Dordrecht, Netherlands: Springer.
- Larson, M. F. (2000). A shear instability seeding mechanism for quasiperiodic radar. Journal of Geophysical Research, 105, 24931–24940.
- Liu, X., Xu, J., Yue, J., Liu, H. L., & Yan, W. (2014). Large winds and wind shears caused by the nonlinear interactions between gravity waves and tidal backgrounds in the mesosphere and lower thermosphere. *Journal of Geophysical Research*, 119, 9. https://doi.org/10.1002/2014JA020221
- Loftness, M. O. (1997). Power line RF interference Sounds, patterns, and myths. *IEEE Transactions on Power Delivery*, 12(2), 934–940. Maeda, J., & Heki, K. (2013). Two-dimensional observations of midlatitude sporadic E irregularities with a dense GPS array in Japan. *Radio*
- Maeda, J., & Heki, K. (2013). Two-dimensional observations of midlatitude sporadic E irregularities with a dense GPS array in Japan. *Radio Science*, 49(1), 28–35. https://doi.org/10.1002/2013RS005295
- Maeda, J., & Heki, K. (2015). Morphology and dynamics of daytime mid-latitude Sporadic-E patches revealed by GPS total electron content observations in Japan. Earth Planets and Space, 67, 89.
- Malins, J. B., Obenberger, K. S., Taylor, G. B., & Dowell, J. (2019). Three-dimensional mapping of lightning-produced ionospheric reflections. Radio Science, 54(11), 1129–1141. https://doi.org/10.1029/2019RS006857
- Mathews, J. D. (1998). Sporadic E: Current views and recent progress. *Journal of Atmospheric and Solar: Terrestrial Physics*, 60(4), 413–435. Obenberger, K. S., Dao, E., & Dowell, J. D. (2019). Experimenting with frequency-and-angular sounding to characterize traveling ionospheric disturbances using the LWA-SV radio telescope and A DPS4D. *Radio Science*, 54(2), 181–193. https://doi.org/10.1029/2018RS006690
- Obenberger, K. S., Taylor, G. B., Hartman, J. M., Clarke, T. E., Dowell, J., Dubois, A., et al. (2015). Monitoring the sky with the prototype all-sky imager on the LWA1. *Journal of Astronomical Instrumentation*, 4, 1.
- Pakala, W. E., & Chartier, V. L. (1971). Radio noise measurements on overhead power lines from 2.4 to 800 kV. *IEEE Transactions on Power Apparatus and Systems PAS*, 90(3), 1155–1165.
- Proctor, D. E. (1981). VHF radio pictures of lightning flashes to ground. Journal of Geophysical Research, 86, 4041-4071.
- Reinisch, B. W., Galkin, I., Khmyrov, G. M., Kozlov, A. V., Bibl, K., Lisysyan, I. A., et al. (2009). New Digisonde for research and monitoring applications. *Radio Science*, 44, RS0A24. https://doi.org/10.1029/2008RS004115
- Reinisch, B. W., & Huang, X. (1983). Automatic Calculation of Electron Density profiles form digital ionograms, 3, Processing of bottom side ionograms. Radio Science, 18, 447–492.
- Saito, S., Yamamoto, M., Hashiguchi, H., & Maegawa, A. (2006). Observation of three dimensional signatures of quasi-periodic echoes associated with mid-latitude sporadic E layers by MU radar ultra-multi-channel system. *Journal of Geophysical Research*, 33, L14109. https://doi.org/10.1029/2005GL025526
- Stathacopoulos, A. D., & Barry, G. H. (1974). Geometric considerations in the design of communications circuits using field-aligned ionospheric scatter. *Radio Science*, 9(11), 1021–1024. https://doi.org/10.1029/RS009i011p01021
- Whitehead, J. D. (1960). Formation of the sporadic E layer in the temperate zones. *Nature*, 188, 567.
- Whitehead, J. D. (1970). Production and prediction of sporadic E. Reviews of Geophysics and Space Physics, 8, 65–144.
- Whitehead, J. D. (1989). Recent work on mid-latitude and equatorial sporadic E. *Journal of Atmospheric and Solar: Terrestrial Physics*, 51, 401–424.
- Woodman, R. F., Yamamoto, M. S., & Fukao, S. (1991). Gravity wave modulation of gradient drift instabilities in the mid-latitude sporadic E irregularities. *Journal of Geophysical Research*, 18, 1197–1200.
- Yamamoto, M., Komoda, N., Fukao, S., Tsunoda, T., Ogawa, T., & Tsuda, T. (1994). Spatial structure of the E region field-aligned irregularities revealed by the MU radar. *Radio Science*, 29, 337–347.
- Yokoyama, T., Hysell, D. L., Otsuka, Y., & Yamamoto, M. (2009). Three-dimensional simulation of coupled Perkins and Es-layer Instabilities in the nighttime midlatitude Ionosphere. *Journal of Geophysical Research*, 114, A03308. https://doi.org/10.1029/2008JA013789
- Yokoyama, T., & Stolle, C. (2016). Low and midlatitude ionospheric plasma density irregularities and their effects on geomagnetic field. Space Science Reviews, 206(1-4), 495-519.

OBENBERGER ET AL. 17 of 17